Check for updates

Boosting the high-rate performance of lithium-ion battery anodes using MnCo$_2$O$_4$/Co$_3$O$_4$ nanocomposite interfaces

Anubha Tomar,†[a] Chirag Vankani,†[b] Satendra Pal Singh, [ID][c] Martin Winter[b] and Alok Kumar Rai [ID] *[a]

Herein, a mesoporous MnCo$_2$O$_4$/Co$_3$O$_4$ nanocomposite was fabricated using a polyvinylpyrrolidone (PVP)-assisted hydrothermal synthesis method by maintaining only the non-stoichiometric ratio of Mn and Co (2 : 6), leading to an extra phase of Co$_3$O$_4$ coupled with MnCo$_2$O$_4$. Microstructural analysis showed that the obtained sample has a uniform nanowire-like morphology composed of interconnected nanoparticles. The stoichiometric ratio (2 : 4) was maintained to synthesize pure MnCo$_2$O$_4$ for comparative analysis. However, the obtained structure of pure MnCo$_2$O$_4$ was found to be irregular and fragile. After their employment as anode-active materials, the nanocomposite electrode showed superior high rate capability (1043.8 mA h g^{-1} at 5C) and long-term cycling stability (773.6 mA h g^{-1} after 500 cycles at 0.5C) in comparison to the pure MnCo$_2$O$_4$ electrode (771.5 mA h g^{-1} at 5C and 638.9 mA h g^{-1} at 0.5C after 500 cycles). It was believed that the extra phase of Co$_3$O$_4$ may also participate in the electrochemical reactions due to its high electrochemically active nature. Benefiting from the appealing architectural features and striking synergistic effect, the integrated MnCo$_2$O$_4$/Co$_3$O$_4$ nanocomposite anode exhibits excellent electrochemical properties and high cycle stability for LIBs.

1 Introduction

The wide applications of rechargeable lithium-ion batteries (LIBs) demand expansion from portable electronic products to electric vehicles (EVs) and hybrid electric vehicles (HEVs). Graphite is the typical anode material in LIBs.[1,2] Various alternative anode materials with mechanisms other than intercalation are being investigated to provide alternatives to graphite.[3,4] It has been found that conversion mechanism-based ternary transition metal oxides (AB$_2$O$_4$) with a cubic spinel structure belong to a group of anode materials, with interesting performance. More precisely, among various binary transition metal oxides, manganese-based materials exhibit a high specific capacity while being environmentally friendly, naturally abundant and cost-effective.[5] However, when binary manganese oxides are solely used in LIBs as anode materials, they tend to suffer from poor cycling performance due to intrinsical disadvantageous properties such as poor electronic conductivity and large volume variations.[6,7] The replacement of one Co within Co$_3$O$_4$ with Mn leads to the fabrication of a ternary hybrid MnCo$_2$O$_4$ spinel, which is considered to be a highly interesting anode material due to its high theoretical capacity ($\sim$906 mA h g^{-1}) and better electrochemical activity than binary Co$_3$O$_4$ and binary manganese oxides.[8] However, the practical realization of MnCo$_2$O$_4$ is still hindered by challenges such as limited stability, structural collapse and a low cycle life. To alleviate this problem, several attempts have been made in recent years such as structural design, carbon coating, substitutional doping, creation of porosity, *etc.* Apart from these methods, material recombination (MnCo$_2$O$_4$@MnO$_2$, NiO-MnCo$_2$O$_4$, *etc.*) has also been proven to be an effective approach for enhancing the electrochemical performance of MnCo$_2$O$_4$, which can be ascribed to the favorable complementarity and interaction of binary transition metal oxide to the ternary host material, resulting in improved conductivity.[9,10]

In this work, we present the fabrication of a MnCo$_2$O$_4$/Co$_3$O$_4$ nanocomposite using hydrothermal synthesis by maintaining only the non-stoichiometric ratio of Mn and Co, leading to the acquisition of an extra phase of Co$_3$O$_4$ coupled with MnCo$_2$O$_4$. This strategy has been found to be novel in mitigating the volume variations of transition metal oxides.[11,12] Benefitting from the appealing architectural features and striking synergistic effect of two different metal oxides, the integrated MnCo$_2$O$_4$/

[a] *Department of Chemistry, University of Delhi, Delhi-110007, India.*
E-mail: akrai@chemistry.du.ac.in
[b] *MEET Battery Research Center, Institute of Physical Chemistry University of Münster Corrensstr. 46, 48149, Münster, Germany*
[c] *Department of Physics, University of Lucknow, Lucknow 226007, India*
† These authors contributed equally to this paper

Co_3O_4 nanocomposite anode exhibits excellent C-rate performance and long-term cycling stability for LIBs.

2 Experimental

2.1 Material synthesis

A typical hydrothermal synthesis procedure is used in the current work to synthesize active materials for LIB application. Briefly, non-stoichiometric amounts of 2 mM $Mn(NO_3)_2 \cdot 6H_2O$, (Sigma Aldrich, 98%) and 6 mM $Co(NO_3)_2 \cdot 6H_2O$ (Fischer Scientific, 97–101%) were uniformly mixed with 0.3 g of urea (Fischer Scientific, 99%). The non-stoichiometric ratio (2 : 6) was maintained to obtain an extra phase of cobalt oxide in the sample. Furthermore, the above resulting mixture was dissolved in a mixed solution of 40 ml of deionized (DI) water and 30 ml of ethylene glycol under constant stirring at room temperature. Afterwards, 0.5 g of polyvinylpyrrolidone (PVP) was also added to the above solution under continuous magnetic stirring to form a homogeneous solution. Then, the obtained homogeneous solution was transferred to a 100 ml Teflon-lined stainless autoclave and heated at 150 °C for 14 h. After natural cooling to room temperature, the obtained product was centrifuged with absolute ethanol and DI water several times to remove organic impurities followed by drying at 60 °C overnight in a hot air oven. To obtain the hybrid $MnCo_2O_4/Co_3O_4$ nanocomposites, the dried product was further calcined at 400 °C for 3 h in an air atmosphere at a ramping rate of 2 °C min⁻¹. Meanwhile, pure $MnCo_2O_4$ was also synthesized using the same experimental parameters/conditions, except for maintaining the stoichiometric ratio of Mn : Co to 2 : 4 for the purpose of comparison.

2.2 Material characterization

To check the phase purity and crystallinity of the synthesized samples, X-ray diffraction (XRD) patterns were collected using a powder X-ray diffractometer (D8-Discover, Bruker, Germany) with Cu Kα radiation (λ = 0.1406 nm). The surface analysis, distribution of crystallite planes, particle size, detailed microstructural analysis of the calcined samples along with the distribution of elements were investigated using scanning electron microscopy (FE-SEM, Zeiss Gemini SEM 500), transmission electron microscopy (FE-TEM, Technai 200, FEI) and energy dispersive X-ray spectroscopy (EDX) interfaced with FE-SEM. To analyze the surface area and pore size distribution of the synthesized samples in the current work, a BET Micromeritics Instrument Corp. Gemini-V instrument, using nitrogen adsorption/desorption isotherms, was employed. The chemical composition and oxidation state of the elements in the synthesized products of the current work were determined by XPS using M/s Thermo Fischer Scientific Instrument UK with a monochromatic Al Kα X-ray source.

2.3 Electrode fabrication

To investigate the electrochemical performance of the synthesized anode materials mentioned above, the fabricated anodes were paired against lithium metal foil in a half-cell configuration, where lithium metal foil served as both the counter and reference electrode. In order to prepare the working electrodes, a paste was first prepared by mixing 60 wt% of active material, 20 wt% carbon black (SuperC65, Imerys Graphite & Carbon) as a conductive agent and 20 wt% poly(vinylidene difluoride) (PVdF, Solef 5130, Solvay) as a binder in N-methyl-2-pyrrolidone (NMP, anhydrous, purity: 99.5%, Sigma-Aldrich) solvent. The obtained paste was then cast on a copper foil (current collector; purity: 99.999%) using the doctor blade technique and the electrode sheets were dried in an atmospheric oven at 70 °C for 2 h. Afterwards, the dried electrode sheets were roll-pressed to improve the contact between the copper current collector and the electrode dry film. The electrodes were punched to a diameter of 14 mm and dried in a Büschi B-585 glass drying oven under reduced pressure ($< 5 \times 10^{-2}$ bar) at 120 °C for 12 h. The active mass loading of the electrode was *ca.* 0.30 mg cm⁻² corresponding to an aerial capacity of 0.27 mA h cm⁻². CR2032 coin-type half-cells were assembled by placing a polypropylene separator (Celgard 2500, 16 mm in diameter) between the working electrode (14 mm) and lithium metal foil (15 mm) soaked with 50 μL of electrolyte consisting of 1 M $LiPF_6$ in ethylene carbonate (EC): dimethyl carbonate (DMC) with a volume ratio of 1 : 1, serving as the electrolyte. The cell assembly was conducted in a dry room atmosphere with a dew point below −50 °C. The electrochemical testing of these assembled half-cells was performed on a Maccor series 4000 battery test system at 20 °C within the potential range of 0.01–3.0 V *vs.* Li⁺/Li at various current rates.

3 Results and discussion

3.1 Physiochemical properties

Fig. 1(a) shows the XRD patterns of both pure $MnCo_2O_4$ and $MnCo_2O_4/Co_3O_4$ nanocomposite samples. Both samples displayed the same diffraction patterns that can be well indexed with a pure cubic phase of $MnCo_2O_4$ (JCPDS no. 01-1130, $Fd\bar{3}m$ space group and lattice parameters a = 8.2 Å). Since pure Co_3O_4 is perfectly isostructural (JCPDS no. 42-1467) to $MnCo_2O_4$, it is difficult to separately identify and index the peaks corresponding to Co_3O_4 in the XRD pattern. In order to determine the actual lattice parameters of $MnCo_2O_4$ and $MnCo_2O_4/Co_3O_4$ nanocomposite samples, we performed Lebail refinement using the Fullprof Program[13] as shown in Fig. 1(b) and (c). The Lebail refinement was carried using a cubic structure in the $Fd\bar{3}m$ space group using a Pseudo-Voigt function, and a linear interpolation between a set background points with refinable heights for profile shape and the background, respectively, was utilized. The lattice parameter obtained from the Lebail refinement was found to be 8.113(1) and 8.0815(7) Å for $MnCo_2O_4$ and $MnCo_2O_4/Co_3O_4$, respectively. The lattice parameter of $MnCo_2O_4$ is larger than that of Co_3O_4 due to the presence of Mn ions with larger ionic radius. Furthermore, in the case of $MnCo_2O_4/Co_3O_4$, the lattice parameter decreases to 8.0815(7) due to the increase in concentration of Co ions having smaller ionic radii than Mn ions. This is evidenced by a slight shift in the XRD pattern
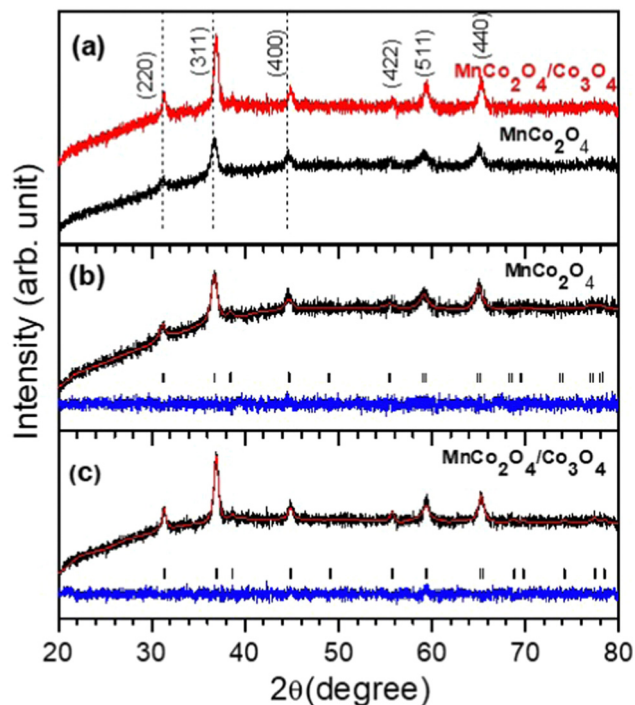
This journal is © the Owner Societies 2024

Phys. Chem. Chem. Phys., 2024, **26**, 3516–3524 | **3517**

Fig. 1 (a) XRD patterns of MnCo₂O₄ and MnCo₂O₄/Co₃O₄ samples. (b) and (c) shows the Lebail refinement on the XRD pattern of MnCo₂O₄ and MnCo₂O₄/Co₃O₄, respectively. The black line, red line and blue line, represent the experimental, calculated and the difference profile, respectively, and vertical tick marks above the difference profile show the Bragg's peak positions.

(shown by dotted lines in Fig. 1(a)) towards higher 2θ values due to the increase in the lattice parameter.

The structural morphology of pure MnCo₂O₄ and MnCo₂O₄/Co₃O₄ nanocomposite samples were analyzed using FE-SEM, FE-TEM, and HR-TEM micrographs, as shown in Fig. 2. It can be noticed that FE-SEM micrographs of pure MnCo₂O₄ (Fig. 2a) exhibit an irregular morphology along with the existence of broken nanowires and some plate-like structures, while the MnCo₂O₄/Co₃O₄ nanocomposite sample (Fig. 2d) clearly shows a uniform nanowire-like structure, which may be due to the presence of an extra phase of Co₃O₄ in the sample, along with MnCo₂O₄. On the other hand, the FE-TEM images of both pure MnCo₂O₄ and MnCo₂O₄/Co₃O₄ nano-composite samples, displayed in Fig. 2(b and e), show similar morphological patterns as observed in SEM analysis. FE-TEM studies confirmed that both the morphologies are composed of interconnected nano-particles with a particle size of ∼15–26 nm for pure MnCo₂O₄ and ∼8–30 nm for MnCo₂O₄/Co₃O₄ nanocomposite samples. However, in comparison to the nanocomposite sample, the morphology of the pure MnCo₂O₄ sample is clearly cracked and fragile with a high agglomeration of nano-particles, which may contribute to the poor electrochemical performance. HR-TEM analysis of both pure MnCo₂O₄ and MnCo₂O₄/Co₃O₄ nanocomposite samples is displayed in Fig. 2(c and f), respectively. Both samples unveil lattice fringes with inter-planar spacings of ∼0.47 nm and ∼0.29 nm, corresponding to (111) and (220) planes of MnCo₂O₄. Furthermore, a representative energy

dispersive X-ray (EDX) spectrum of MnCo₂O₄/Co₃O₄ nanocomposite sample is also provided to analyze the elemental composition in the sample, as shown in Fig. 2(g–i). The elemental mapping results indicate the homogeneous distribution of only Mn, Co, and O in the sample, again confirming the purity of the sample.

Nitrogen adsorption–desorption isotherm test was further conducted to investigate the specific surface area and porosity of both pure MnCo₂O₄ and MnCo₂O₄/Co₃O₄ nanocomposite samples. Both the samples displayed a type IV curve with an H3 hysteresis loop, suggesting the existence of mesoporosity in the samples, as depicted in Fig. 3(a and b). The specific surface area of both pure and nanocomposite samples was measured to be ∼64.6 m² g⁻¹ and ∼46.5 m² g⁻¹, respectively. Insets of Fig. 3(a and b) show the pore size distribution curve obtained by the Barret–Joyner–Halenda (BJH) method. The total pore volume and average pore diameters were around ∼0.085 cm³ g⁻¹ and ∼5 nm for the pure sample and ∼0.123 cm³ g⁻¹ and ∼10 nm for nanocomposite samples.

A representative X-ray photoelectron spectroscopy (XPS) analysis was carried out to examine the surface compositions, bonding configurations and oxidation state of the ions present in the MnCo₂O₄/Co₃O₄ nanocomposite sample and the obtained results are shown in Fig. 4. The full survey spectrum, as shown in Fig. 4(a), confirmed the existence of Mn, Co, O and C elements in the sample. The C peak is frequently used in XPS as a charge correction reference for convenience. Moreover, all three spectra of Mn-2p, Co-2p and O-1s were separately fitted using XPSPEAK 41 software against a linear-type background for detailed analysis. The high-resolution Mn-2p spectra (Fig. 4b) exhibit peaks at binding energies of ∼642.0 eV and ∼653.6 eV, corresponding to $2p_{3/2}$ and $2p_{1/2}$ of Mn²⁺, respectively, while the peaks located at ∼644.2 eV and ∼656.1 eV can be attributed to $2p_{3/2}$ and $2p_{1/2}$ of Mn³⁺, respectively.[14–17] Fig. 4(c) shows the Co-2p spectrum, with peaks located at binding energies of ∼780.0 eV and ∼781.6 eV for $2p_{3/2}$ and ∼795.0 eV and ∼796.7 eV for $2p_{1/2}$, indicating the existence of Co²⁺, and Co³⁺, respectively.[14–17] On the other hand, the two shakeup peaks observed at around ∼788.2 eV and ∼804.1 eV are the satellite peaks that appeared for Co-2p, denoted as "Sat." in the figure. Fig. 4(d) illustrates the high resolution O-1s spectrum, which is deconvoluted into three peaks at binding energies of ∼530.1 eV (O 1), ∼530.6 eV (O 2) and ∼531.9 eV (O 3), corresponding to the lattice oxygen in metal–oxygen bonds (Mn–O and Co–O), the oxygen in hydroxyl groups, and the water molecules adsorbed on the surface, respectively.[14,18] The obtained results conclude that the surface of the MnCo₂O₄/Co₃O₄ nanocomposite sample exhibits the coexistence of electron couples of Mn³⁺/Mn²⁺ and Co³⁺/Co²⁺.

3.2 Electrochemical performance

In order to further investigate the electrochemical behavior of both pure MnCo₂O₄ and MnCo₂O₄/Co₃O₄ nanocomposite samples as LIB anodes, cyclic voltammetry (CV) was initially performed at different scan rates of 0.1, 0.2, 0.5, 1, 1.5, and 2 mV s⁻¹ in the potential range of 0.01–3.0 V (*vs.* Li/Li⁺). It can be clearly
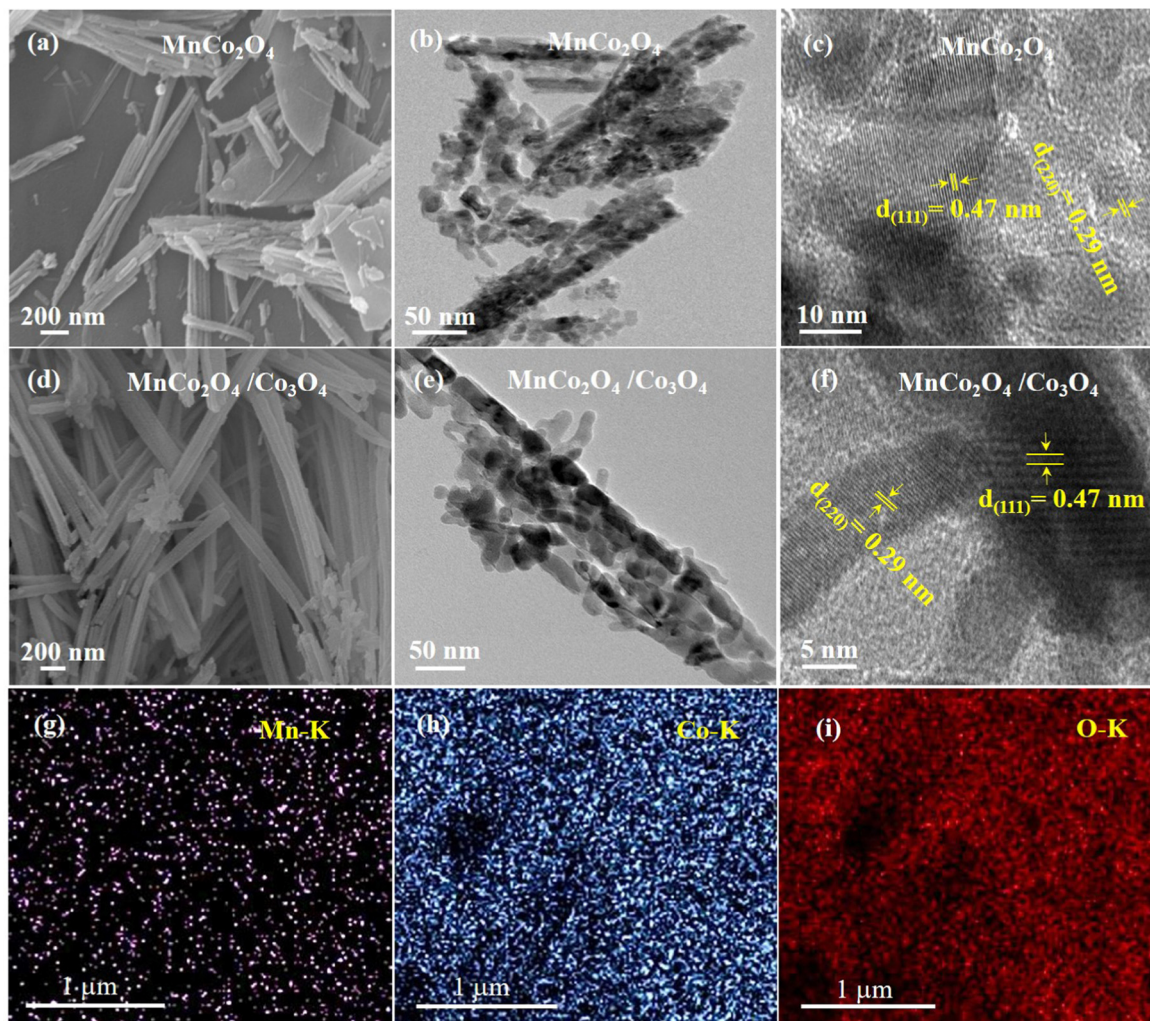
3518 | *Phys. Chem. Chem. Phys.*, 2024, **26**, 3516–3524

This journal is © the Owner Societies 2024

Fig. 2 (a) and (d) FE-SEM images; (b) and (e) FE-TEM images; and (c) and (f) HR-TEM images of pure $MnCo_2O_4$ and $MnCo_2O_4/Co_3O_4$ nanocomposite samples, respectively; (g)–(i) representative energy dispersive X-ray elemental mapping images of the $MnCo_2O_4/Co_3O_4$ nanocomposite sample.
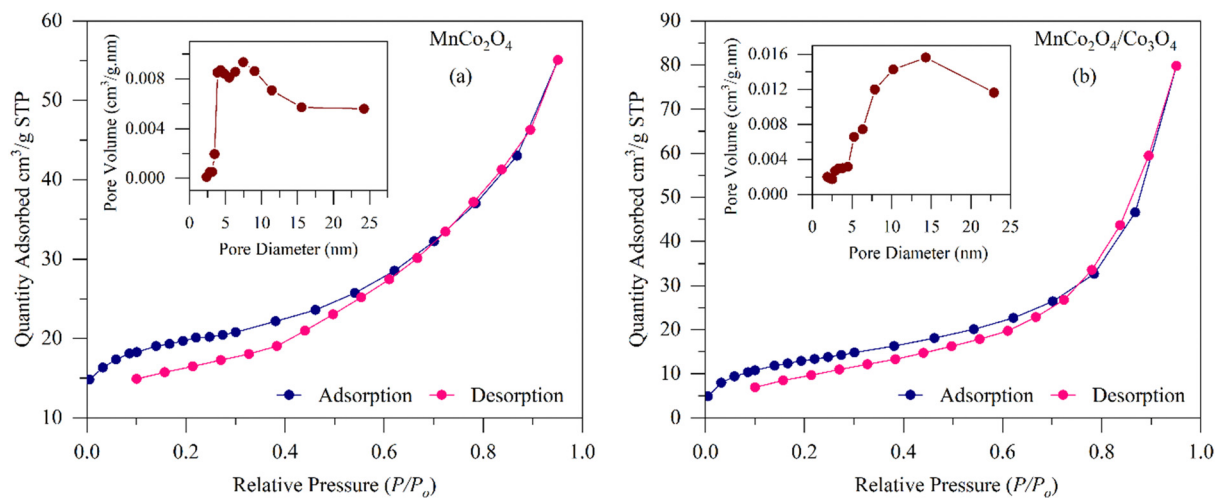

Fig. 3 N_2 adsorption–desorption isotherms with corresponding BJH pore size distribution curves (inset) of (a) pure $MnCo_2O_4$ and (b) $MnCo_2O_4/Co_3O_4$ nanocomposite samples.
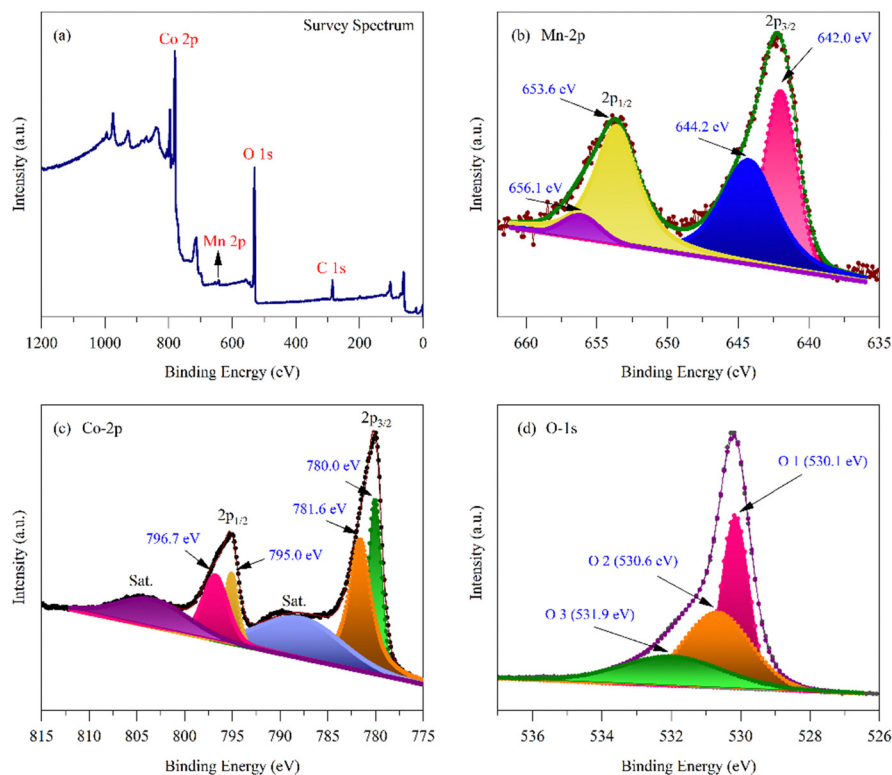
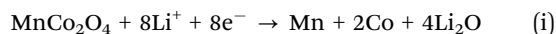**Fig. 4** A representative XPS spectra of the $MnCo_2O_4/Co_3O_4$ nanocomposite sample: (a) survey spectrum; (b) Mn-2p, (c) Co-2p, and (d) O-1s.

observed from Fig. 5(a and b) that both the electrodes exhibit broad reduction peaks at ~0.67 V and ~0.52 V, respectively, during all cathodic scans, which is due to the reduction of metal ions, i.e., Co^{3+} is transformed into Co^{2+}, followed by the further reduction of both Co^{2+} and Mn^{2+} to metallic Co and Mn along with the formation of amorphous Li_2O.[15,19,20] However, during the anodic scans, two broad oxidation peaks were found at ~1.6 V/~2.1 V, and ~1.45 V/~2.1 V for pure $MnCo_2O_4$ and $MnCo_2O_4/Co_3O_4$ nanocomposite electrodes, which can be ascribed to the oxidation of Mn and Co to Mn^{2+} and Co^{2+}, respectively.[15,19,20] In addition, all the CV curves display the similar shape with a nominal shift of the reduction and oxidation peaks under various scan rates ranging from 0.1 to 2 mV s^{-1}, indicating that both the active materials exhibit highly reversible redox reactions. Based on the above analysis and previous reports, the entire electrochemical reaction mechanism can be expressed using the following equations:[21–24]

$$MnCo_2O_4 + 8Li^+ + 8e^- \rightarrow Mn + 2Co + 4Li_2O \qquad (i)$$

$$Co_3O_4 + 8Li^+ + 8e^- \rightarrow 3Co + 4Li_2O \qquad (ii)$$

$$Mn + 2Co + 3Li_2O \leftrightarrow MnO + 2CoO + 6Li^+ + 6e^- \qquad (iii)$$

The lithium storage mechanism was further quantified by a power relationship between the measured peak current (i) and scan rate (v) using following eqn (iv) and (v):[25,26]

$$i = av^b \qquad (iv)$$

$$\log(i) = b \cdot \log(v) + \log(a) \qquad (v)$$

The 'b' value can be obtained from the slope of the linear relationship between $\log(i)$ and $\log(v)$, as depicted in Fig. 5(c and d). The 'b' value helps in determining the Li^+ storage behavior of the battery. In general, the Li^+ storage process within the battery follows two mechanisms: (i) the diffusion-controlled process (battery behavior) and (ii) the surface capacitive-controlled process (pseudo capacitance behavior), which can be determined by the 'b' value.[27,28] Fig. 5(c and d) shows the fitted 'b' values for the cathodic/anodic peaks of both pure $MnCo_2O_4$ and $MnCo_2O_4/Co_3O_4$ nanocomposite electrodes, which are around ~0.775/0.628 and ~0.748/0.667, respectively. Since the 'b' values are between 0.5 and 1, it is believed that both the mechanisms take part in the Li^+ storage process. It is well-known that the high specific capacity results from the diffusion contribution, whereas the excellent rate capability is attributed to its surface contribution.[29] Thereafter, the contributions of diffusion controlled and surface-controlled mechanisms were calculated using the following eqn (vi) and (vii):[30]

$$i(V) = k_1v + k_2v^{1/2} \qquad (vi)$$

$$i(V)/v^{1/2} = k_1v^{1/2} + k_2 \qquad (vii)$$

where $i(V)$ is the current at constant potential. k_1v and $k_2v^{1/2}$ represent the contributions of surface-controlled and diffusion-controlled processes, respectively. On the other hand, the slope (k_1) and intercept (k_2) values can be obtained by linear fitting of $i(V)/v^{1/2}$ versus $v^{1/2}$ at a constant potential, using eqn (vii). The percentage contribution ratio of surface-controlled and diffusion- controlled mechanisms for both pure $MnCo_2O_4$

3520 | Phys. Chem. Chem. Phys., 2024, **26**, 3516–3524
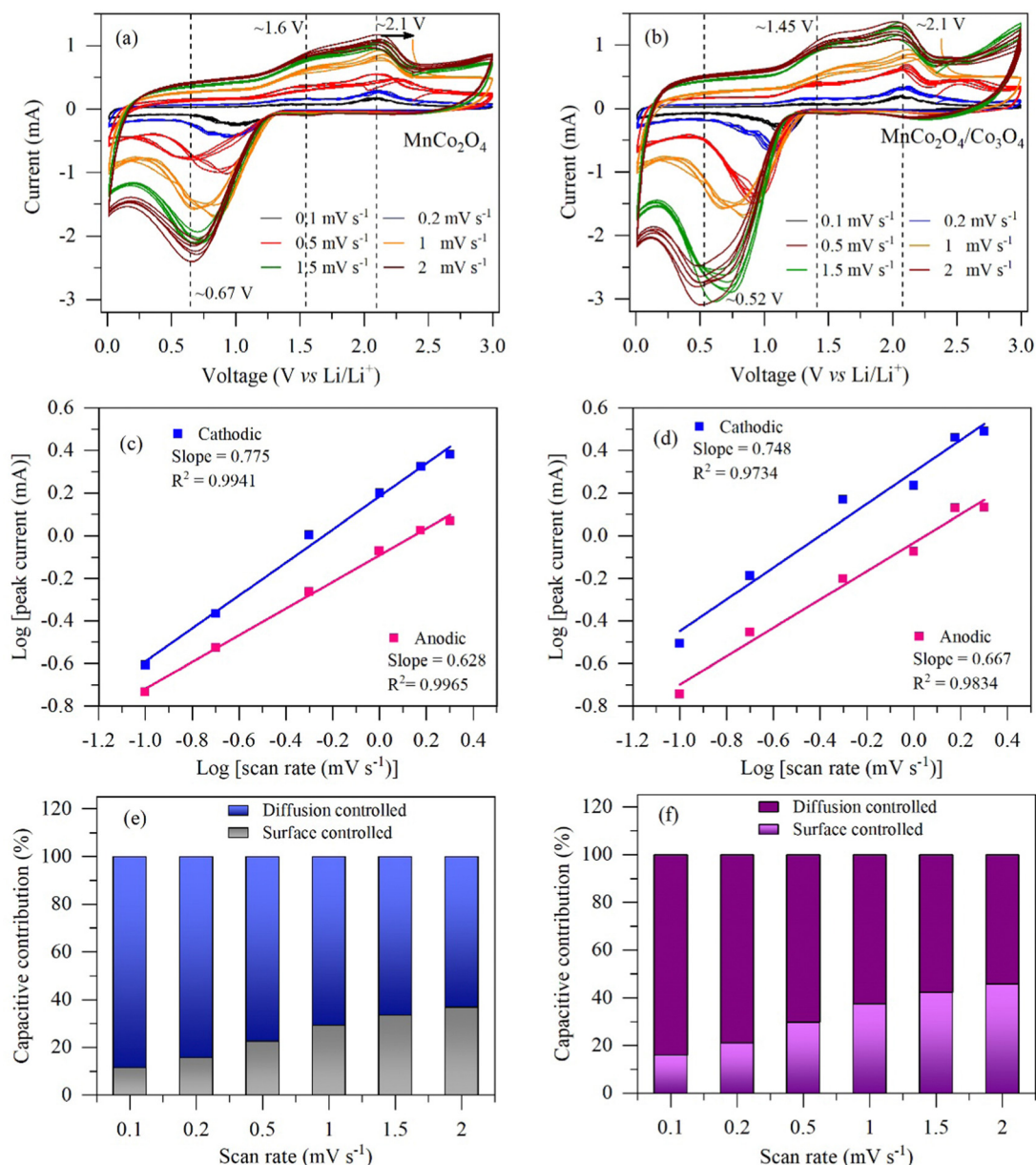
This journal is © the Owner Societies 2024

Fig. 5 (a) and (b) Cyclic voltammetry curves at various scan rates; (c) and (d) linear relationship between the logarithm of peak current and scan rates; and (e) and (f) the corresponding capacitive and diffusion contribution ratio at different scan rates for pure MnCo$_2$O$_4$ and MnCo$_2$O$_4$/Co$_3$O$_4$ nanocomposite samples, respectively.

and MnCo$_2$O$_4$/Co$_3$O$_4$ nanocomposite electrodes at various scan rates of 0.1, 0.2, 0.5, 1, 1.5 and 2 mV s^{-1} are summarized in Fig. 5(e and f). It can be seen that the pseudocapacitance contribution (surface-controlled capacitive) for both electrodes increases with the increase in scan rates. Remarkably, the MnCo$_2$O$_4$/Co$_3$O$_4$ nanocomposite electrode exhibits a higher capacitive contribution than the pure MnCo$_2$O$_4$ electrode at high scan rates, which can be ascribed to the fast Li$^+$-ion insertion–de-insertion reactions.

Fig. 6(a and b) shows the galvanostatic 1st, 2nd, 50th and 100th charge–discharge curves for pure MnCo$_2$O$_4$ and MnCo$_2$O$_4$/Co$_3$O$_4$ nanocomposite electrodes at a constant current rate of 0.5C (1C = 906 mA h g^{-1}) under the voltage window

of 0.01 to 3 V (vs. Li/Li$^+$). The initial charge–discharge capacities were measured to be 897.2/963.1 for pure and 919.7/958.7 mA h g^{-1} for the nanocomposite electrode with corresponding Coulombic efficiencies of ∼93.1% and ∼95.9%, respectively. Both electrodes showed long discharge and charge voltage plateaus at ∼1.1 V and ∼2.1 V, which can be attributed to the reversible reduction and oxidation of Mn^{2+} and Co^{2+} to metallic Co and Mn and vice versa, respectively. The obtained results are in good agreement with the CV results. Although the obtained initial capacities are higher than the theoretical capacities of both MnCo$_2$O$_4$ (906 mA h g^{-1}) and Co$_3$O$_4$ (890 mA h g^{-1}), the additional irreversible discharge capacity observed in the first cycle could be mainly due to the formation of solid electrolyte
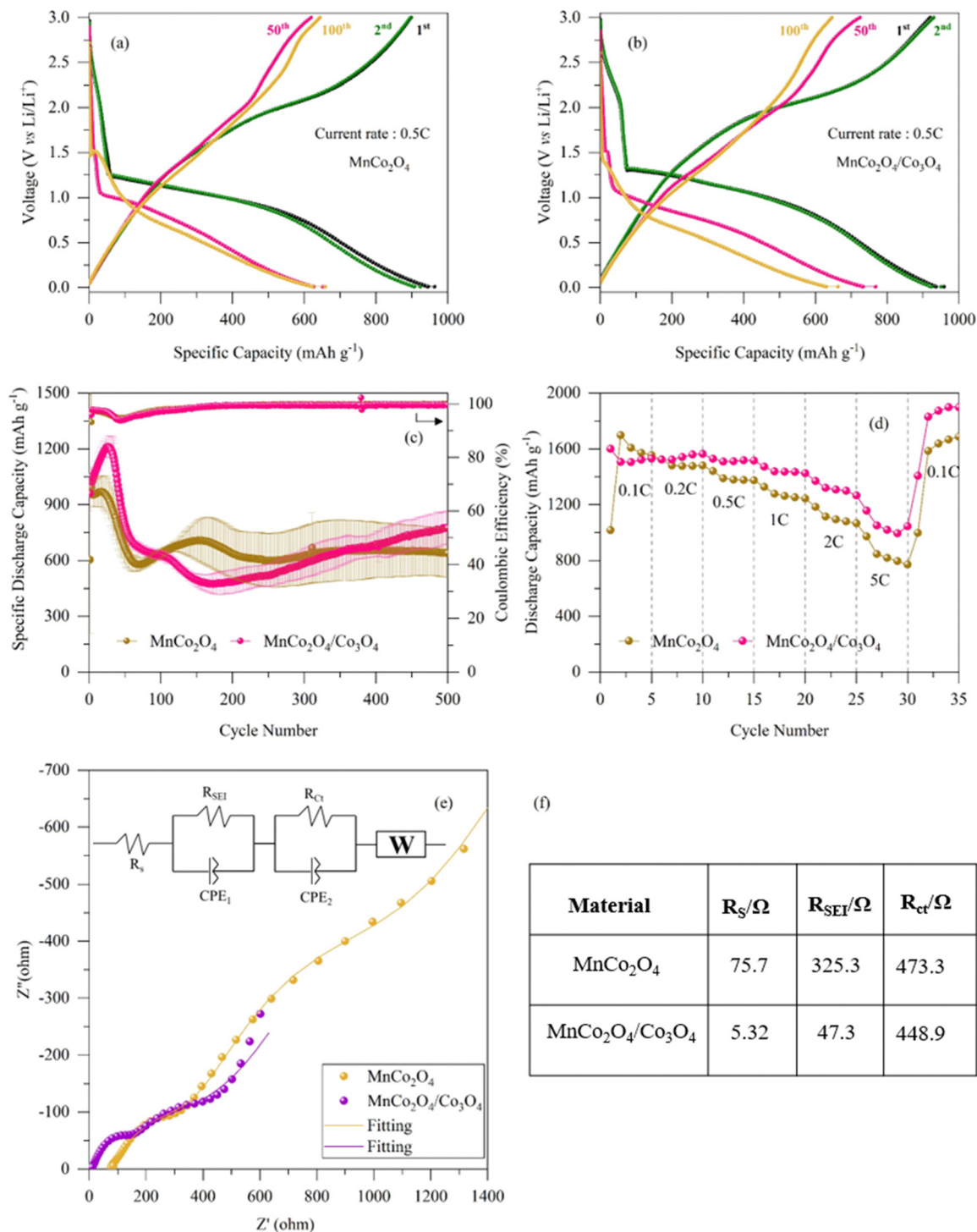
This journal is © the Owner Societies 2024

Phys. Chem. Chem. Phys., 2024, **26**, 3516–3524 | **3521**

Fig. 6 (a) and (b) Charge–discharge curves at 0.5C; (c) cycling performances for 500 cycles; and (d) rate performance at various C-rates of pure $MnCo_2O_4$ and $MnCo_2O_4/Co_3O_4$ nanocomposite electrodes, respectively; (e) EIS spectra of pure $MnCo_2O_4$ and $MnCo_2O_4/Co_3O_4$ nanocomposite electrodes after 500 cycles; and (f) fitting parameter values from an equivalent circuit model.

Material	R_S/Ω	R_{SEI}/Ω	R_{ct}/Ω
$MnCo_2O_4$	75.7	325.3	473.3
$MnCo_2O_4/Co_3O_4$	5.32	47.3	448.9

interphase (SEI) films on the electrode surface through electro-lyte decomposition.[19] Subsequently, the $MnCo_2O_4/Co_3O_4$ nano-composite electrode delivered charge–discharge capacities of 929.5/950.2, 723.9/767.4 and 645.7/662.5 mA h g^{-1} for 2nd, 50th, and 100th cycles, which are significantly higher than

those of the pure $MnCo_2O_4$ electrode (896.07/923.4, 618.5/651.6 and 643.1/657.8 mA h g^{-1}) obtained for the same cycles, respectively. It can be seen that the specific capacity achieved in the 100th cycle by the $MnCo_2O_4/Co_3O_4$ nanocomposite elec-trode is still higher than that of the pure $MnCo_2O_4$ electrode,

3522 | *Phys. Chem. Chem. Phys.*, 2024, **26**, 3516–3524

This journal is © the Owner Societies 2024

which indicates that the nanocomposite electrode has high potential to sustain during long-term cycling.

Fig. 6(c) shows the long-term cycling performance of both the electrodes at 0.1C for the first two cycles and then at 0.5C for consecutive 500 cycles. In order to activate and stabilize the material, the first two cycles of both the electrodes were performed at a low current rate of 0.1C. Initially, both pure $MnCo_2O_4$ and $MnCo_2O_4/Co_3O_4$ nanocomposite electrodes exhibit a gradual increase in the capacity till 18th and 28th cycles, respectively. Furthermore, as the cycle number increases, both the electrodes show unusual behavior with a significant decline in the capacity until 200 cycles, which later gradually increases. This behavior is usually seen in most of the transition metal oxide anode materials due to the formation of an unstable polymeric gel-like film resulting from the partial decomposition of electrolyte. As the cycles progress, the formation of a stable SEI film occurs, which allows the uniform penetration of the electrolyte, resulting in enhanced Li^+ diffusion kinetics due to the gradual activation of the electrode material and thereby increasing the capacity in the subsequent cycles.[31–33] It can be noted that the $MnCo_2O_4/Co_3O_4$ nanocomposite electrode delivered a maximum capacity of 773.6 mA h g^{-1} after 500 cycles, which is nearly double of the capacity of the pure $MnCo_2O_4$ electrode (638.9 mA h g^{-1}) at the same cycle. The obtained high capacity of the nanocomposite electrode can be ascribed to the combined effect of $MnCo_2O_4$ and Co_3O_4, which seems to provide multiple benefits such as inhibiting the volume variations during insertion–de-insertion of Li^+ ions, improving the structural stability of the electrode material, increasing the active sites for Li^+ diffusion and providing a synergistic effect to maintain the mechanical stability of the electrode material during repeated cycling.

The rate capability performance of pure $MnCo_2O_4$ and $MnCo_2O_4/Co_3O_4$ nanocomposite electrodes is further tested and compared at various C-rates ranging from 0.1C to 5C, as displayed in Fig. 6(d). At various C-rates of 0.1C, 0.2C, 0.5C, 1C, 2C and 5C, the nanocomposite electrode obviously delivers higher discharge capacities of 1529.7, 1562.9, 1514.7, 1424.2, 1264.7 and 1043.8 mA h g^{-1} than the pure electrode (1554.9, 1480.5, 1373.1, 1242.9, 1065.5 and 771.5 mA h g^{-1}) at same C-rates, respectively. More importantly, after the current was restored to 0.1C, both pure $MnCo_2O_4$ and $MnCo_2O_4/Co_3O_4$ nanocomposite electrodes recovered even high discharge capacities of 1686.5 and 1898.3 mA h g^{-1}, respectively, than before. It can be seen that the nanocomposite electrode exhibits superior rate performance compared to the pure electrode, which is not only due to the high uniformity in the morphology but also due to the presence of an extra phase of Co_3O_4, resulting in the high structural integrity of the nanocomposite electrode during fast Li^+-ion insertion–de-insertion reactions. In contrast, the irregular morphology of pure $MnCo_2O_4$, without the presence of any extra support to sustain the structure, leads to structural degradation during repetitive insertion–de-insertion of Li^+ ions.

To gain further insight into the electrical conductivity, EIS analysis was performed on the cycled electrodes of pure $MnCo_2O_4$ and $MnCo_2O_4/Co_3O_4$ nanocomposite after 500 cycles and the obtained Nyquist plot is displayed in Fig. 6(e). It can be noted that the Nyquist plot of both the electrodes exhibits two depressed semicircles in the high to medium frequency region, followed by an inclined line in the low-frequency region. The equivalent circuit, given in the inset of Fig. 6(e), was employed to fit these semicircles and the obtained fitted impedance parameters are summarized in Fig. 6(f). The notation mentioned in the equivalent circuit such as R_s, R_{SEI}, R_{ct} and W, represents the electrolyte resistances, the SEI film resistance, the charge transfer resistance at the electrode/electrolyte interface and the diffusion resistance of Li^+ ions into the electrode material, respectively.[14,34,35] As per the fitting results, the $MnCo_2O_4/Co_3O_4$ nanocomposite electrode shows lower values of R_s, R_{SEI}, and R_{ct} compared to the pure $MnCo_2O_4$ electrode, which consequently proves the highly beneficial effect of the extra phase of Co_3O_4 in the nanocomposite sample, resulting in improved conductivity, facile charge transfer and high Li^+-ion diffusion.

Conclusions

In this work, we have fabricated $MnCo_2O_4/Co_3O_4$ nanocomposite samples using a facile hydrothermal synthesis method by maintaining only the nonstoichiometric ratio of Mn and Co precursors and employed them as anode materials for LIB applications. To compare the performance of the nanocomposite electrode, pure $MnCo_2O_4$ was also prepared using the same synthesis parameters, with the exception of using the stoichiometric ratio of Mn and Co precursors. The $MnCo_2O_4/Co_3O_4$ nanocomposite electrode exhibited excellent electrochemical performance compared to the pure $MnCo_2O_4$ electrode. It is believed that the high synergistic effect between $MnCo_2O_4$ and Co_3O_4 in the nanocomposite sample not only improves conductivity and provides more active sites for Li^+-ion diffusion, but also accelerates the charge transfer kinetics in the material. More importantly, at a high current rate of 5C, the $MnCo_2O_4/Co_3O_4$ nanocomposite electrode exhibits a discharge capacity of 1043.8 mA h g^{-1}, which is not only higher than that of the pure electrode (771.5 mA h g^{-1} at 5C) but also higher than the theoretical capacity of $MnCo_2O_4$ (1C = 906 mA g^{-1}), suggesting that the Co_3O_4 phase may also take part in the electrochemical reactions, improving the total capacity of the host material.

Conflicts of interest

There are no conflicts to declare.

Acknowledgements

This journal is © the Owner Societies 2024

Phys. Chem. Chem. Phys., 2024, **26**, 3516–3524 | **3523**

References

1 A. Jain, B. J. Paul, S. Kim, V. K. Jain, J. Kim and A. K. Rai, *J. Alloys Compd.*, 2019, **772**, 72–79.

2 D. S. Baji, S. V. Nair and A. K. Rai, *J. Solid State Electrochem.*, 2017, **21**, 2869–2875.

3 T. D. Hatchard and J. R. Dahn, *J. Electrochem. Soc.*, 2004, **151**, A838–A842.

4 G. Derrien, J. Hassoun, S. Panero and B. Scrosati, *Adv. Mater.*, 2007, **19**, 2336–2340.

5 M. Wang, Y. Huang, Y. Zhu, M. Yu, X. Qin and H. Zhang, *Composites, Part B*, 2019, **167**, 668–675.

6 J. Jiang, Y. Li, J. Liu, X. Huang, C. Yuan and X. W. D. Lou, *Adv. Mater.*, 2012, **24**, 5166–5180.

7 A. L. M. Reddy, S. R. Gowda, M. M. Shaijumon and P. M. Ajayan, *Adv. Mater.*, 2012, **24**, 5045–5064.

8 K. Zhong, X. Xia, B. Zhang, H. Li, Z. Wang and L. Chen, *J. Power Sources*, 2010, **195**, 3300–3308.

9 Y. Zhu, Y. Huang and M. Wang, *Chem. Eng. J.*, 2019, **378**, 122207.

10 T. Li, X. Li, Z. Wang, H. Guo, Q. Hu and W. Peng, *Electrochim. Acta*, 2016, **191**, 392–400.

11 A. Tomar, E. Adhitama, M. Winter, T. Placke and A. K. Rai, *Batteries Supercaps*, 2023, **6**, e202200465.

12 M. X. Li, Y. X. Yin, C. J. Li, F. Z. Zhang, L. J. Wan, S. L. Xu and D. G. Evans, *Chem. Commun.*, 2012, **48**, 410–412.

13 Rodriguez-Carvajal, J. FullProf; Laboratoire Léon Brillouin, CEA-CNRS CEA/Saclay: 91191; Gif sur Yvette Cedex: France, 2008.

14 L. Q. Fan, J. L. Huang, Y. L. Wang, C. L. Geng, S. J. Sun, Y. F. Huang, J. M. Lin and J. H. Wu, *Int. J. Hydrogen Energy*, 2021, **46**, 35330–35341.

15 C. Chen, B. Liu, Q. Ru, S. Ma, B. An, X. Hou and S. Hu, *J. Power Sources*, 2016, **326**, 252–263.

16 D. S. Baji, H. S. Jadhav, S. V. Nair and A. K. Rai, *J. Solid State Chem.*, 2018, **262**, 191–198.

17 P. Kulkarni, D. Ghosh, G. Balakrishna, R. S. Rawat, S. Adams and M. V. Reddy, *Ceram. Int.*, 2019, **45**, 10619–10625.

18 H. S. Jadhav, A. Roy, W. J. Chung and J. G. Seo, *Electrochim. Acta*, 2017, **246**, 941–950.

19 T. Li, X. Li, Z. Wang, H. Guo, Q. Hu and W. Peng, *Electrochim. Acta*, 2016, **191**, 392–400.

20 L. Zhang, Q. Tang, X. Chen, B. Fan, K. Xiao, S. Zhang, W. Deng and A. Hu, *J. Alloys Compd.*, 2017, **722**, 387–393.

21 G. Huang, S. Xu, Z. Xu, H. Sun and L. Li, *ACS Appl. Mater. Interfaces*, 2014, **6**, 21325–21334.

22 L. Li, Y. Q. Zhang, X. Y. Liu, S. J. Shi, X. Y. Zhao, H. Zhang, X. Ge, G. F. Cai, C. D. Gu, X. L. Wang and J. P. Tu, *Electrochim. Acta*, 2014, **116**, 467–474.

23 G. Li, L. Xu, Y. Zhai and Y. Hou, *J. Mater. Chem. A*, 2015, **3**, 14298–14306.

24 K. Jang, D. K. Hwang, F. M. Auxilia, J. Jang, H. Song, B. Y. Oh, Y. Kim, J. Nam, J. W. Park, S. Jeong, S. Lee, S. Choi, I. S. Kim, W. B. Kim, J. M. Myoung and M. H. Ham, *Chem. Eng. J.*, 2017, **309**, 15–21.

25 Z. Wu, Y. Wang, Z. Liu, Y. Li, X. Lai, X. Ma, S. Yang and X. Yan, *J. Mater. Sci.*, 2022, **57**, 9389–9402.

26 J. Deng, X. Yu, Y. He, B. Li, Q. H. Yang and F. Kang, *Energy Storage Mater.*, 2017, **6**, 61–69.

27 L. Zhu, F. Li, T. Yao, T. Liu, J. Wang, Y. Li, H. Lu, R. Qian, Y. Liu and H. Wang, *Energy Fuels*, 2020, **34**, 11574–11580.

28 J. L. Niu, C. H. Zeng, H. J. Peng, X. M. Lin, P. Sathishkumar and Y. P. Cai, *Small*, 2017, **13**, 1702150.

29 D. P. Dutta, D. D. Pathak, S. Abraham and B. R. Ravuri, *RSC Adv.*, 2022, **12**, 12383–12395.

30 B. Jiang, C. Han, B. Li, Y. He and Z. Lin, *ACS Nano*, 2016, **10**, 2728–2735.

31 C. Wu, Y. Xu, L. Ao, K. Jiang, L. Shang, Y. Li, Z. Hu and J. Chu, *J. Alloys Compd.*, 2020, **816**, 152627.

32 L. Chen, Y. Huang, Y. Chen, L. Zheng, Y. Zhao, Y. Chen, G. Zhao, J. Li, Y. Lin and Z. Huang, *J. Mater. Sci.*, 2021, **56**, 9356–9367.

33 Z. Dai, Z. Long, R. Li, C. Shi, H. Qiao, K. Wang and K. Liu, *ACS Appl. Energy Mater.*, 2020, **3**, 12378–12384.

34 Z. Zhang, J. Liang, X. Zhang, W. Yang, X. Dong and Y. Jung, *Int. J. Hydrogen Energy*, 2020, **45**, 8186–8197.

35 J. Li, S. Xiong, X. Li and Y. Qian, *Nanoscale*, 2013, **5**, 2045–2054.